Impact of invasive metal probes on Hall measurements in semiconductor nanostructures

Gluschke, Jan G.; Seidl, Jakob; Tan, H. Hoe; Jagadish, Chennupati; Caroff, Philippe; Micolich, Adam P.

DOI
10.1039/d0nr04402d

Publication date
2020

Document Version
Final published version

Published in
Nanoscale

Nanoscale

PAPER

View Article Online
View Journal | View Issue

Cite this: *Nanoscale*, 2020, **12**, 20317

Impact of invasive metal probes on Hall measurements in semiconductor nanostructures†

Jan G. Gluschke,[a] Jakob Seidl,[a] H. Hoe Tan,[b] Chennupati Jagadish,[b] Philippe Caroff[b,c] and Adam P. Micolich *[a]

Received 10th June 2020,
Accepted 27th August 2020

DOI: 10.1039/d0nr04402d

rsc.li/nanoscale

Recent advances in bottom-up growth are giving rise to a range of new two-dimensional nanostructures. Hall effect measurements play an important role in their electrical characterization. However, size constraints can lead to device geometries that deviate significantly from the ideal of elongated Hall bars with currentless contacts. Many devices using these new materials have a low aspect ratio and feature metal Hall probes that overlap with the semiconductor channel. This can lead to a significant distortion of the current flow. We present experimental data from InAs 2D nanofin devices with different Hall probe geometries to study the influence of Hall probe length and width. We use finite-element simulations to further understand the implications of these aspects and expand their scope to contact resistance and sample aspect ratio. Our key finding is that invasive probes lead to significant underestimation of measured Hall voltage, typically of the order 40–80%. This in turn leads to a subsequent proportional overestimation of carrier concentration and an underestimation of mobility.

1. Introduction

The Hall effect[1] has a long history, both as a source of novel states of matter, *e.g.*, the integer,[2] fractional,[3] and spin[4] Hall effects, and as an essential characterization tool for semiconducting materials.[5] Hall studies are particularly amenable to the recent explosion of 2D nanomaterials that began with graphene,[6,7] extended into transition metal dichalcogenides,[8,9] *e.g.*, MoS_2,[10,11] $MoSe_2$,[12] WS_2,[10] and WSe_2,[13] and has most recently moved to III–V semiconductors[14–24] aiming to meet the demand for more complex III–V nanostructure geometries in fields such as quantum computing.[25–29]

We have recently worked on one of the new 2D morphologies of III–V semiconductors emerging from advances in bottom-up growth approaches. Our selective-area epitaxy-grown InAs 2D nanofins are rectangular—typically a few microns long and wide, and 50–100 nm thick.[14] Electrical contacts for device characterization are fabricated with electron-beam lithography and subsequent metal deposition. Hall probes made in this way overlap with the nanostructure and are typically a few hundred nanometres wide. This is significant compared to the size of the nanostructure. Fig. 1a shows a typical device.

This Hall effect geometry is far from the ideal of a high aspect ratio (length ≫ width), rectangular 'Hall bar' with recessed, non-invasive, currentless Hall voltage probes that are well separated from the source and drain contacts.[5] Instead, in 2D nanomaterial Hall devices, the aspect ratio is low because it is determined by the intrinsic nanostructure geometry and is often closer to 1. Furthermore, the metal Hall probes overlapping the conduction channel form a parallel current path through the nanostructure segment, which perturbs the current density. These non-idealities influence the result of a Hall voltage measurement but are generally ignored in the characterization studies of new 2D nanomaterials. This can lead to a significant misestimate of Hall voltage, and subsequently, the extracted material parameters such as carrier density and mobility. It is thus important to systematically study and quantify the impact of non-idealities in 2D nanostructure Hall devices to correct for their impact and enable more accurate material characterization.

Here, we systematically investigate the impact of sample and contact geometry for 2D nanomaterials with invasive metal contacts on classical Hall effect measurements. We used InAs nanofin Hall devices with multiple Hall probe pairs to measure the effect of contact geometry on a single nanofin. We obtained up to 2.5-fold differences in measured Hall

[a]*School of Physics, University of New South Wales, Sydney, NSW 2052, Australia. E-mail: adam.micolich@nanoelectronics.physics.unsw.edu.au*
[b]*Department of Electronic Materials Engineering, Research School of Physics, The Australian National University, Canberra, ACT 2601, Australia*
[c]*Microsoft Quantum Lab Delft, Delft University of Technology, 2600 GA, Delft, The Netherlands*

† Electronic supplementary information (ESI) available: Estimate of the effect of probe side facet coverage. Simulations of recessed Hall probes. Estimate of the effect of additional Hall probes on Hall voltage measurement. Table with simulated Hall voltages for additional sample geometries. See DOI: 10.1039/d0nr04402d

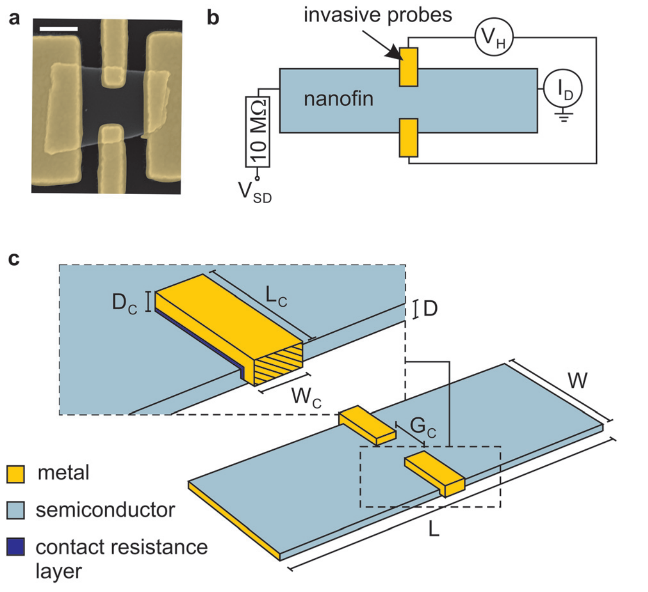

Fig. 1 (a) Scanning electron microscopy (SEM) image of a typical nanofin device with two metal Hall probes (scale bar = 500 nm). (b) Schematic of the electrical measurement circuit. (c) Schematic of a model approximating a nanofin device in our simulations defining the width W, length L and height D of the 2D structure as well as the width W_C, length L_C, and height D_C of the probes. The gap between the Hall probes is G_C. Note that W_C runs perpendicular to W and L_C runs perpendicular to L for convenience of discussion.

voltage for different contact geometries of the same device. We extend our experimental study using finite-element modelling to better understand and quantify the impact of sample aspect ratio, contact resistance and the width and length of the Hall probes.

Based on our data, we provide recommendations on how to design devices to reduce current perturbation and how to estimate a Hall voltage correction factor for non-ideal devices. We estimate that direct Hall voltage measurements on typical 2D nanostructure devices with invasive contacts underestimate the real Hall voltage by around 40–80%. This leads to a proportional overestimation of carrier concentration and underestimation of the carrier mobility.

2. Methods

2.1 Nanofin growth and device processing

InAs nanofins with high aspect ratio were chosen to isolate the impact of invasive probes on Hall measurements from the effects arising from the nanofin geometry. Full details are given in ref. 14, but briefly, the nanofins are 1.05 μm wide and approximately 5 μm long, 70–110 nm thick and grown on an InP(111)B substrate by metal–organic vapor phase epitaxy. The growth was templated by pre-patterned trenches defined by electron beam lithography and dry-etching in a SiO_x mask layer on the substrate.[14] Individual nanofins were carefully mechanically transferred to a Si device substrate with a 100 nm SiO_2 layer and prefabricated alignment markers. Electrical contacts were patterned using electron-beam lithography. The contact regions were exposed to a 30 s oxygen plasma etch (350 mTorr, 50 W) to remove resist residue and then to an $(NH_4)_2S_x$ passivation solution at 40 °C for 120 s immediately prior to contact metal deposition to remove native oxides and improve ohmic contact formation.[30] The contact metal (Ni/Au 5/135 nm) was deposited by thermal evaporation. Narrow probe leads can suffer discontinuities during lift-off reducing their yield. The devices were inspected under a scanning electron microscope (SEM) prior to electrical characterization to confirm contact alignment. Care was taken to limit the electron beam exposure during SEM to avoid significant changes in electrical characteristics.[31,32]

2.2 Electrical characterization

Fig. 1b shows a schematic of the measurement configuration. Hall voltage V_H data were obtained using SR830 lock-in amplifiers with a current I_D of 77 Hz between the source and drain, which is passed *via* a 10 MΩ series resistor to maintain a constant current of 100 nA (typical sample resistance ∼5 kΩ). Measurements were performed with the device at a temperature of 20 K to prevent strong quantum conductance fluctuations[14] from obscuring the Hall data. We used an Oxford Instruments Heliox VL ^{3}He system with a 2 T magnet in a Wessington CH-120 helium dewar to achieve this.

2.3 Finite-element modelling

The simulations were performed using COMSOL Multiphysics 5.1 with the electric currents (ec) module in a stationary study. The nanofin was modelled as a cuboid with length L = 5 μm, width W = 1 μm and thickness D = 75 nm unless otherwise specified. The structure was assigned the anisotropic conductivity tensor:[5]

$$\sigma = \mu ne \begin{pmatrix} \frac{1}{1+\mu^2B^2} & -\frac{\mu B}{1+\mu^2B^2} & 0 \\ \frac{\mu B}{1+\mu^2B^2} & \frac{1}{1+\mu^2B^2} & 0 \\ 0 & 0 & 1 \end{pmatrix} \tag{1}$$

with carrier mobility μ, carrier concentration n, electron charge e and magnetic field B.[33] We chose μ = 3100 cm^2 (V s)$^{-1}$ and $n = 2 \times 10^{17}$ cm^{-3} as default values based on our earlier study on InAs 2D nanofins.[14] However, the effects leading to a reduced measured Hall voltage discussed in this paper only depend on the device geometry and the ratio of the sample conductivity to the Hall probe conductivity, and not on the specific values of n and μ. We expect our model to hold for all devices for which the Drude approximation, *i.e.*, eqn (1), is valid.

Fig. 1c shows a schematic of a modelled device with one pair of metallic Hall probes of contact length L_C and width W_C. The gap between the two probes is $G_C = W - 2L_C$. The contact height D_C is fixed at 100 nm. The contacts were assigned an isotropic conductivity of $\sigma_C = 8.5 \times 10^8$ S m^{-1} to approximate commonly used Au contacts.[34] This is approximately 5 orders of magnitude higher than the nanofin conductivity. The finite thickness of the nanofins inevitably means that the contacts on the top surface need to step down the edges onto the substrate to continue to the external circuitry. We find that the extent of side facet coverage does not have a significant impact on the modelled Hall voltage (see the ESI Fig. S1†). We chose the Hall probes in the simulation to extend half-way down the side of the nanofin to account for the side facet geometry in our InAs nanofins. Note that the reduction in Hall voltage extracted from the simulation depends on the relative rather than the absolute dimensions of the simulated device. This means that the considerations presented for *e.g.* 5 μm × 1 μm equally apply for 50 nm × 10 nm devices provided that all other dimensions (*e.g.* Hall probes) are scaled accordingly.

A 10 nm layer with an isotropic conductivity of $\sigma_{CR} \le \sigma_C$ was placed between the metal contact and the semiconductor structure to model contact resistance (blue in Fig. 1c). However, we considered no contact resistance, $\sigma_{CR} = \sigma_C$, as our default case unless specified otherwise. The two surfaces at the ends of the nanofin were modelled as electrical terminals with the source supplying a constant current I_D = 100 nA and the drain set at 0 V. The outer side of each Hall contact was set as a floating potential to extract the Hall voltage (shaded area in Fig. 1c). We used B = 0.1 T unless otherwise indicated and the simulations were computed to a relative tolerance of 10^{-5}.

2.4 Clarification of terminology

In this paper, we discuss three different Hall voltages. The 'real' Hall voltage V_H^{real} is calculated analytically from the input parameters I_D, B, n, and D:[5]

$$V_H^{real} = \frac{I_D B}{nDe}. \tag{2}$$

This is the Hall voltage value that, by definition, yields the correct carrier concentration. We use it to normalise our other two Hall voltages V_H^{sim} and V_H^{exp} for clearer analysis. The second is the Hall voltage V_H^{sim} extracted from the simulations. The model simulates a measurement where V_H^{sim} is the difference in the electrical potential of two Hall probes. Some models in section 3.2 and 3.3 do not have Hall probes. Here, V_H^{sim} corresponds to the potential difference between two points at the modelled sample's edge. The third Hall voltage is the measured Hall voltage V_H^{exp}, which is obtained directly from the experimental measurements performed on real samples. If a measurement or simulation is 'ideal', then we obtain $V_H^{sim}/V_H^{real} = V_H^{exp}/V_H^{real}$ = 1. Deviations from 1 indicate non-ideality. R_H^{sim}, R_H^{exp} and R_H^{real} are the corresponding Hall coefficients.

3. Results and discussion

3.1 Hall effect measurements in practice

Sample and Hall-probe geometry can both vary widely in the characterization of 2D nanostructures. The high aspect ratio of our selective-area epitaxy-grown nanofins (5 μm × 1 μm) allows the placement of multiple Hall probes with differing probe gap G_C and width W_C. This enables us to measure V_H^{exp} for

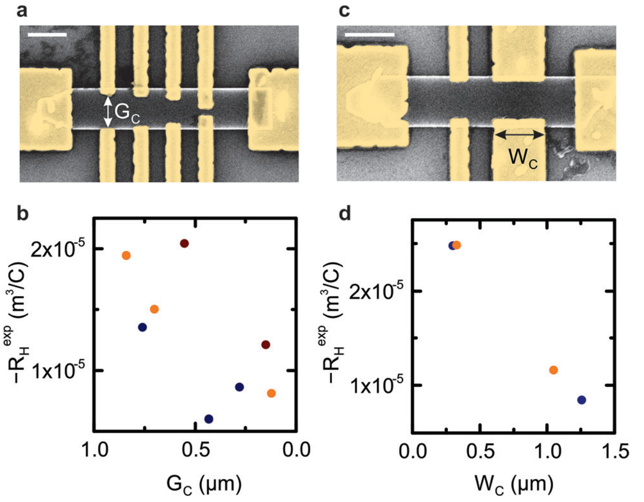

Fig. 2 (a) SEM image of a nanofin device with four independent pairs of Hall probes for testing the effect of probe gap G_C (scale bar = 1 μm). (b) Negative of the measured Hall coefficient $-R_H^{exp}$ *vs.* G_C for three different devices represented by different colours (device from (a) shown in orange). (c) SEM image of a nanofin device with two independent pairs of Hall probes for testing the effect of contact width W_C (scale bar = 1 μm). (d) $-R_H^{exp}$ *vs.* W_C for two different devices (device from (c) shown in orange). The data point width is equal to the uncertainty in G_C and W_C, respectively.

different probe geometries without the effect of sample-to-sample variations. Fig. 2a shows a device with four Hall probes. All contacts are ~350 nm wide but the gap between the probes G_C varies between 120 and 840 nm. For an ideal Hall device, all the probes should measure the same Hall voltage. Fig. 2b shows that this is not the case. The absolute value of the measured Hall coefficient $-R_H^{exp} = -V_H^{exp} D/(I_D B)$ is significantly smaller for the probe pairs with smaller gaps across all three devices (different colour data points in Fig. 2b).

Fig. 2c shows a device with probe pairs of different width W_C. The measured Hall coefficients for different W_C are shown in Fig. 2d. The magnitude of R_H^{exp} is almost three times larger for the narrow probe pair in both measured devices, despite the contact gap G_C being the same. This would yield a nearly three-fold difference in extracted carrier concentrations for the same sample. The measurements demonstrate that probe geometry has a significant impact on the outcome of a Hall measurement. In the following sections, we use finite-element modelling to investigate the impact of contact and sample geometries on probed Hall voltage.

3.2 Sample geometry

Fig. 3 gives an overview of how different sample and contact geometries influence the simulated Hall voltage V_H^{sim} at the probes. All extracted Hall voltages were normalized to V_H^{real}, such that an ideal modelled Hall device would return V_H^{sim}/V_H^{real} = 1. Geometry A is a 'contactless' 5 μm × 1 μm rectangular sample with V_H^{sim} extracted directly from the electrical potential difference between the two points at the centre of the side surfaces. We obtain $V_H^{sim} = V_H^{real}$ here, as expected. We obtain the same

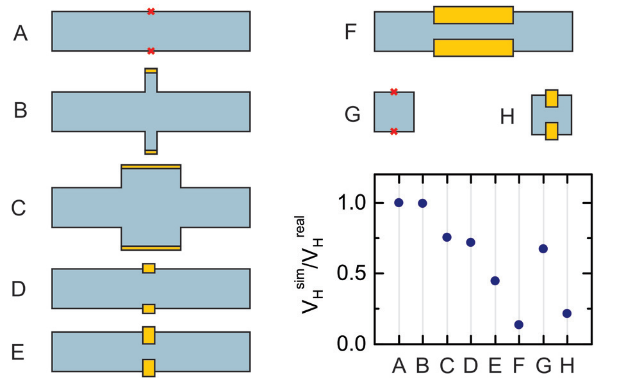

Fig. 3 Simulation of the Hall voltage V_H^{sim} for different device and contact geometries: high aspect ratio nanofins with 'ideal' contactless probes (A), a classic Hall bar (B), wide recessed Hall probes (C), device with short metal probes (D), long metal probes (E), wide metal probes (F), low aspect-ratio nanofin with 'ideal' contactless probes (G), and invasive contacts (H). V_H^{sim} is normalized to the 'real' Hall voltage V_H^{real}.

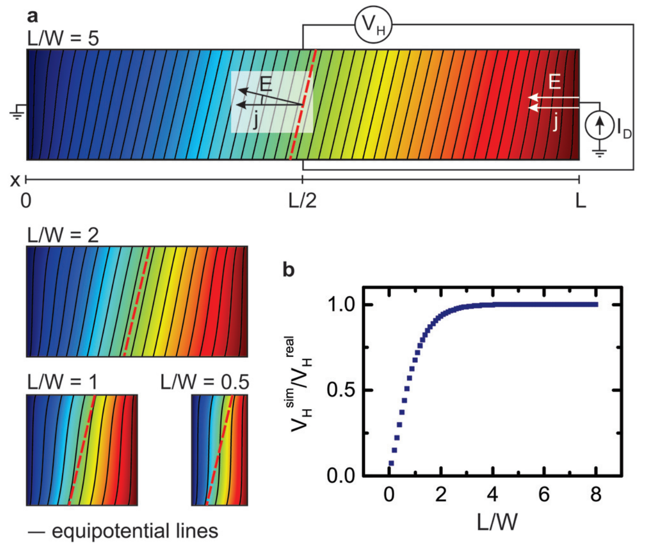

Fig. 4 (a) Equipotential lines for four different *L*/*W* aspect ratio samples at magnetic field *B* = 0.75 T. The red dashed line indicates an equipotential line corresponding to the Hall angle of V_H^{real}. (b) Transverse voltage drop V_H^{sim} at the sample's centre normalized to V_H^{real} *vs.* sample aspect ratio *L*/*W*.

result for the traditional Hall bar geometry with currentless recessed contacts (Geometry B). In contrast, Geometries D–F feature invasive metal contacts overlapping the semiconductor channel. Here, the simulations show that V_H^{sim} is significantly smaller than V_H^{real}. The reduction is particularly pronounced for the wide contacts in Geometry F where V_H^{sim} is less than 15% of V_H^{real}. This would lead to an underestimation of carrier concentration by a factor of >6 in a real measurement. Note that recessed probes also become invasive if the probes are sufficiently short and wide relative to the sample dimensions (Geometry C). Such geometries are relevant to, *e.g.*, nanocross devices[27,35] and are discussed in section 3.5 and in detail in the ESI S2–S3.†

In Geometries G and H, we consider the effect of reducing the aspect ratio *L*/*W*, which further lowers V_H^{sim}. We find a 30% reduction in Hall voltage even without invasive probes (G) for a sample with an aspect ratio of 1. In the following subsections, we will examine the factors causing the reduction in Hall voltage more closely.

3.3 Sample aspect ratio

Probing of the Hall voltage too close to the source and drain contacts leads to an underestimate of the Hall voltage.[5,36] This is why the Hall probes are separated from the source and drain probes by at least four times the width of the sample in ideal Hall bar devices.[5,36] Good geometric control is often not achieved in many 2D nanostructures. This leads to measurements with low aspect ratio and poor probe separations being used. A quantitative estimate of the reduction in Hall voltage due to a reduced sample aspect ratio is thus necessary to correct these measurements.

Fig. 4a shows the electrical equipotential lines of samples with different aspect ratios *L*/*W* in a simulated Hall measurement at a magnetic field *B* = 0.75 T. The source and drain contacts force the interface at both ends to be at a fixed potential (0 V and V_{SD}, respectively). Here, the electric field *E* is parallel to the current density *j* and both are perpendicular to the contact interface. The equipotential lines gradually turn as one moves closer to the sample centre until *E* is at the Hall angle $\Theta = \tan^{-1}(\mu B)$ relative to *j* in the middle of the Hall bar. The Hall voltage at any position *x* along the sample is the transverse potential difference between the two edges at *x*. The red dashed line indicates an equipotential line corresponding to the Hall angle of V_H^{real}. If V_H^{sim} is probed too close to the source and drain contacts, then V_H^{sim} is significantly smaller than V_H^{real}. This matters for low aspect ratio samples because the length is insufficient for *E* to align with the 'real' Hall angle at the position *x* where the contacts are located. In Fig. 4b, we plot the ratio V_H^{sim}/V_H^{real} using the potential difference between opposite edges at $x = L/2$ to identify the aspect ratio where non-ideality becomes significant. We find that the expected Hall voltage V_H^{sim} is within 1% of V_H^{real} for an aspect ratio *L*/*W* above 3.3 and within 10% for aspect ratio above 1.8. The reduction in V_H^{sim} is more than 30% for aspect ratios below 1, *i.e.*, samples with $L < W$. The effect can be further compounded by the effect of metal probes as we see in section 3.4. The simulations in the following sections will focus on samples with high aspect ratio of 5 to isolate the effects of invasive probes from those of sample geometry.

3.4 Invasive metal contacts

A homogeneous current density is assumed when evaluating a Hall measurement. Recessed, currentless Hall probes are used in traditional Hall bars to ensure that the voltage probes do not interfere with the sample current. Fig. 5a shows the modelled current density (red arrows) through a traditional Hall bar confirming there is no significant current perturbation. This is not the case for 'invasive' metal probes that overlap the

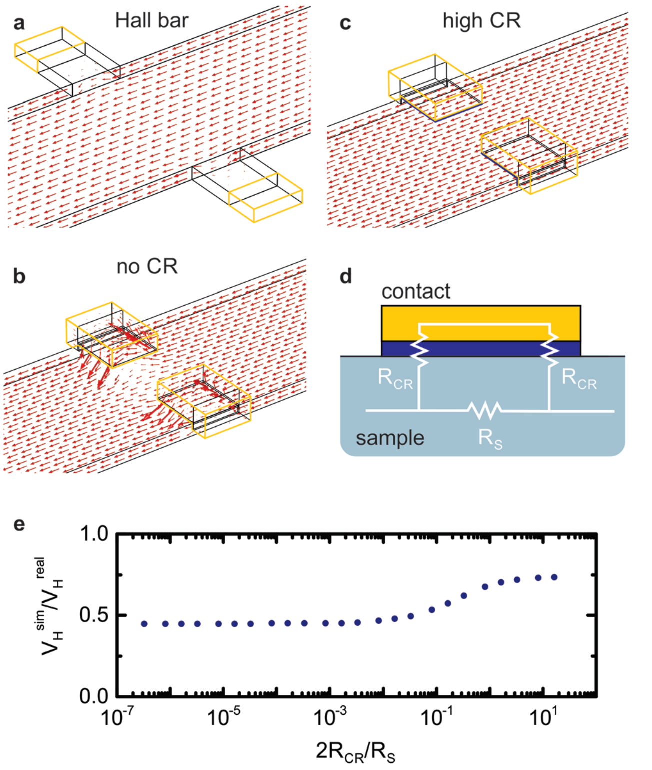

Fig. 5 Simulation of current density (red arrows) in (a) a classic Hall bar, (b) sample with 'invasive' low contact resistance metal probes, and (c) sample with high contact resistance metal probes. (d) Schematic of the two competing current paths through the sample and the contact in the probed segment. R_{CR} is the contact resistance and R_S is the resistance of the segment below the contact. (e) V_H^{sim}/V_H^{real} for different contact $2R_{CR}/R_S$ ratios.

conduction channel and are used in the characterization of many 2D nanostructures; see Fig. 5b, where the metal contacts are traced in yellow for clarity. The simulation shows a clear reduction in current density between and beneath the metal contacts. This occurs because the contacts themselves provide the lowest resistance path through this sample segment. The resulting perturbation of the current density significantly reduces V_H^{sim}.

In our simulation, we use the 10 nm thin interface layer between the nanofin and the metal contact to simulate contact resistance. This enables us to vary the resistance of the current path through the contact. A simplified model of the two current paths through the probed nanofin segment is shown in Fig. 5d. We estimate the contact resistance R_{CR} as the resistance of the 10 nm layer with conductivity σ_{CR} and area A_{CR} so that $R_{CR} = 10\ \text{nm}/(\sigma_{CR}{\cdot}A_{CR})$. We compare this to the resistance $R_S = W_C/(\mu ne{\cdot}L_C{\cdot}D)$ of the sample segment immediately below the contact. Fig. 5e shows V_H^{sim}/V_H^{real} *versus* $2R_{CR}/R_S$, providing a rough estimate of the ratio of the resistances of the two current paths. The reduction of the Hall voltage is the largest when $R_{CR} \ll R_S$. This means that the current path through the contact is the path of lowest resistance (see Fig. 5b). The Hall voltage increases as $2R_{CR}/R_S$ approaches 1 and saturates for $R_{CR} \gg R_S$, where current no longer flows through the Hall probes. This case is shown in Fig. 5c. In this regime, the potential sensed by each voltage probe is the average electric potential at the nanofin–probe interface. The probed Hall voltage V_H^{exp} or V_H^{sim} is then the potential difference between the two Hall probes. The real Hall voltage V_H^{real} can therefore be estimated using:

$$V_H^{real} \approx V_H^{exp/sim} \Big/ \left(0.5 + \frac{G_C}{2W}\right). \quad (3)$$

We find that the measured Hall voltage is approximately 50% of V_H^{real} for low to moderate contact resistances and just over 70% for high contact resistances for this particular geometry (W_C = 300 nm, G_C = 400 nm). In other words, high contact resistance probes make the Hall voltage measurement more accurate and easier to interpret because V_H^{real} can be estimated using eqn (3). The contact resistances are generally very low in a material with a prominent surface accumulation layer like InAs.[37] Thus, the resulting current distortion effects need to be taken into account. The impact of the current distortion effects on the Hall measurement is not straightforward and depends on multiple parameters—most significantly on probe width and length as we will discuss in section 3.6.

3.5 Recessed Hall probes

We saw in Fig. 5a that the use of recessed Hall probes in classical Hall bar devices eliminates the current perturbation effect. In this case, the recessed contact length L_{RC} is large compared to the recessed contact width W_{RC}. Furthermore, W_{RC} is much smaller than the device dimensions L and W. Some nanoscale devices such as nanocrosses[27,35] feature recessed contacts but do not always fulfil the conditions above. Here, L_{RC} may be less than W_{RC} and $W_{RC} \approx W$. In this case, current perturbation effects can occur as we observed above for metal contacts that overlap the semiconductor channel. Fig. 6a and b show the simulations of current density for two 5 µm × 1 µm Hall devices with 0.5 and 0.1 µm long and 1 µm wide recessed Hall probes with metal contacts (yellow) at the end. The current density is significantly reduced at the device centre for the

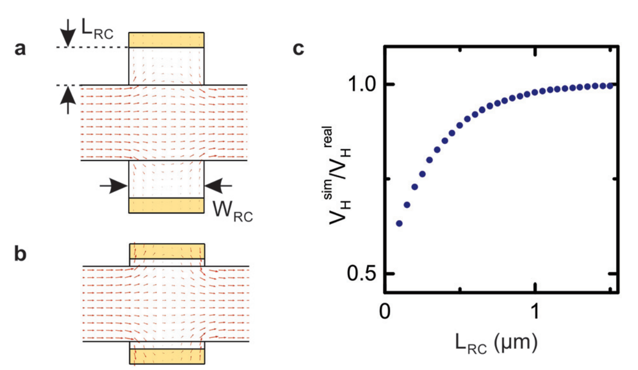

Fig. 6 Simulated current density for a 5 µm × 1 µm nanofin with 1 µm wide and (a) 0.5 µm and (b) 0.1 µm long recessed contacts. (c) V_H^{sim}/V_H^{real} *vs.* recessed contact length L_{RC} for this device geometry.

device with L_{RC} = 0.1 µm as current is diverted through the contacts. Fig. 6c shows that this leads to a reduction in V_H^{sim}, as we saw for metal contacts that overlap the channel. The resistance of the current path through the contacts rises as L_{RC} is increased and the current perturbation is reduced. For this particular geometry, $V_H^{sim}/V_H^{real} \approx 0.98$ for L_{RC} = 1 µm. A more comprehensive discussion of recessed contacts and the simulations of a range of device geometries are provided in the ESI.† Overall, recessed Hall probes give significantly more accurate Hall voltage measurements than metal probes with channel overlap. However, current perturbation effects should be considered in samples with $2L_{RC} < W_{RC}$ and where W_{RC} is of the order of W and L.

3.6 Metal probe geometry

Fig. 7a shows the simulations of V_H^{sim}/V_H^{real} for 5 µm long samples as a function of Hall–probe gap G_C normalized to the sample width W of 1 µm. We first consider contacts with limited invasiveness. The 300 nm wide probe pair with high contact resistance (red, σ_{CR} = 10 S m^{-1}) and the 10 nm wide probe pair (yellow) both start at $V_H^{sim}/V_H^{real} \approx 1$ for $G_C/W = 0$ and linearly decrease to $V_H^{sim}/V_H^{real} \approx 0.5$ at $G_C/W = 1$. This behaviour is approximated well by eqn (3), which is plotted as a grey line. Wider invasive contacts exhibit a different behaviour (green W_C = 0.3 µm, blue W_C = 1 µm). V_H^{sim}/V_H^{real} is significantly smaller than 1 for $G_C/W = 1$, where the Hall probes only contact the side walls of the sample. This is due to the current perturbation effect discussed in section 3.4. We will examine this more closely in Fig. 7b.

Fig. 7b shows V_H^{sim}/V_H^{real} as a function of probe width W_C. The Hall voltage should not depend on contact width in devices with non-invasive probes. This is consistent with the modelling of high contact resistance probes, where we obtain only a weak dependence on W_C (red G_C = 0.4 µm). In stark contrast, V_H^{sim}/V_H^{real} for invasive probes shows a strong dependence on W_C even for very short Hall probe lengths (yellow L_C = 10 nm). This is because wider Hall probes draw more current, reducing the current density at the centre of the sample. For short probe pairs, V_H^{sim} decreases by approximately 50% at $W_C \approx W$, and even more for longer probe pairs (green G_C = 0.8 µm and blue G_C = 0.4 µm). This is particularly relevant for Hall measurements on nanowires where the channel width is often equal to or smaller than the probe width.[31,33,38,39]

Taking the insights gained through the simulations, we can now revisit the experimental data from the devices in section 3.1. Fig. 7c shows the experimentally obtained Hall coefficients R_H^{exp} (circles) together with data from simulations R_H^{sim} (triangles). The model geometry for the simulations is based on the dimensions of the real devices extracted from SEM and atomic-force microscopy (AFM). The model for the device from Fig. 2a is shown in Fig. 7e with a plot of the current density. Note that all probes are included in the model. This is important because the absolute position along the channel and position relative to other probe pairs can impact V_H^{sim} (see the ESI S4†). For our study, it was important to use multiple Hall probe pairs on the same nanofin to isolate the effect of Hall

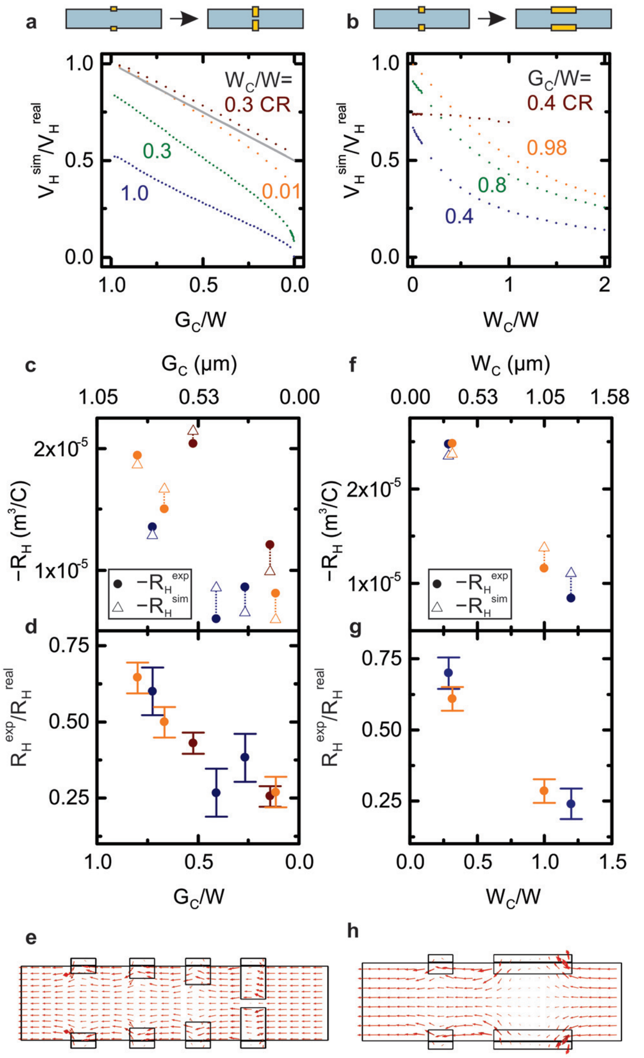

Fig. 7 (a) V_H^{sim}/V_H^{real} *vs.* probe gap per sample width G_C/W for 1 µm (blue), 0.3 µm (green), and 10 nm (orange) wide probes with no contact resistance and 0.3 µm wide probes with high contact resistance (red). The grey line follows eqn (3). (b) V_H^{sim}/V_H^{real} *vs.* contact width per sample width W_C/W for different G_C/W: 0.4 µm (blue), 0.8 µm (green), and 0.98 µm (orange) with no contact resistance, and 0.4 µm with high contact resistance (red). (c) Measured and simulated Hall coefficients R_H^{exp} and R_H^{sim} for different probe gaps G_C from the device presented in Fig. 2. Different devices are represented in different colours. The experimental and the corresponding simulated datapoints are connected by a dashed line for clarity. The carrier concentration for the simulations $n = 1.32 \times 10^{23}$ m^{-3} (red), $n = 2.78 \times 10^{23}$ m^{-3} (blue) and $n = 2.08 \times 10^{23}$ m^{-3} (orange) are based on the least-squares method for the best match of R_H^{exp} and R_H^{sim}. (d) R_H^{exp}/R_H^{real} *vs.* G_C/W where R_H^{real} is based on the carrier concentrations obtained in (c). Error bars are based on the average difference between R_H^{exp} and R_H^{sim} in (c). (e) Simulation of current density for the device depicted in Fig. 2a. (f) R_H^{exp} and R_H^{sim} for devices with different probe widths W_C. R_H^{sim} is based on $n = 1.77 \times 10^{23}$ m^{-3} (blue) and $n = 1.54 \times 10^{23}$ m^{-3} (orange). (g) Corresponding R_H^{exp}/R_H^{real}. (h) Simulation of current density for the device shown in Fig. 2c.

probe geometry from sample-to-sample variations in carrier concentration. We found the best agreement between simulations and experiments occured when using no contact resistance, confirming that the metal probes on InAs are strongly invasive. The carrier concentrations were adjusted in the simulations to match the amplitude of R_H^{exp}. We obtained $n = 1.32 \times 10^{23}$ m^{-3} (red), $n = 2.78 \times 10^{23}$ m^{-3} (blue) and $n = 2.08 \times 10^{23}$ m^{-3} (orange) using the least-squares method. The modelling fits the experimental data well. The average relative difference between the experimental and simulated datapoints is 16%. We attribute the discrepancy to two main factors. First, the shape of the metal contacts in the real devices is slightly irregular with rounded edges and a slightly rugged outline (see Fig. 2a). Second, the simulation assumes a perfectly uniform carrier concentration. In reality, surface accumulation layers[40] and variations in potential landscape, *e.g.*, due to charge trapping[41,42] and polytypism[43,44] likely lead to a more complex carrier distribution in InAs nanostructures. Overall, the data are in good agreement, validating the modelling. This allows us to estimate the ratio of the measured R_H^{exp} and the real Hall coefficient R_H^{real}, with the latter analytically calculated using the carrier concentrations above. Fig. 7d shows R_H^{exp}/R_H^{real} *versus* G_C/W, with error bars based on the average difference between R_H^{exp} and R_H^{sim} in Fig. 7c. We find that R_H^{exp} is 60–70% of R_H^{real} for large probe gaps and as low as 25% for the narrowest probe gaps. The latter would correspond to a four-fold overestimate of carrier concentration and an underestimate of mobility. Specifically, for the device shown in Fig. 2a, we estimate that the real mobility is approximately 2000 cm^2 V^{-1} s^{-1}. Without correction, we would obtain between 500 and 1250 cm^2 V^{-1} s^{-1} depending on which probe pair was used.

We obtain similar results for the two samples with probe pairs of different width W_C. Fig. 7f shows the experimentally obtained data with simulations for $n = 1.77 \times 10^{23}$ m^{-3} (blue) and $n = 1.54 \times 10^{23}$ m^{-3} (orange). The corresponding estimates for R_H^{exp}/R_H^{real} are shown in Fig. 7g and give R_H^{exp}/R_H^{real} as low as 0.25 for wide contacts. The effect of invasive contact width is well illustrated by the simulated current density in Fig. 7h. The current density is significantly diminished between the wide contacts whereas it remains relatively unperturbed for the narrow contact pair.

4. Discussion and conclusion

We have shown that compact sample geometries and invasive metal contacts significantly reduce the measured Hall voltage. This can lead to a substantial overestimate of the nanostructure's carrier density. For a typical 1 μm × 1 μm nanofin with 300 nm × 300 nm overlapping Hall probes, the measured Hall voltage is only ∼20% of V_H^{real} (H in Fig. 3). We identified three contributions to the reduction in Hall voltage: (i) the rotation of the electric field vector to the Hall angle relative to the current density is not completed in low aspect ratio samples, leading to a reduction in Hall voltage; (ii) contacts that draw no current but overlap the conduction channel will measure the average electrical potential of the probe–semiconductor interface, which always yields $V_H^{exp} \leq V_H^{real}$; (iii) metal contacts with low to moderate contact resistance draw current and distort the current density in the nanostructure, which leads to further reduction in measured Hall voltage.

The contribution of (i) only depends on the sample aspect ratio L/W and can therefore be estimated from the simulations provided in Fig. 4. We recommend aiming for devices with an aspect ratio no smaller than 2 to keep the reduction of V_H^{exp} to below 10%. Only one pair of Hall probes should be used at the centre of the device. Multiple Hall probe pairs are convenient for four-probe measurements; however, they often lead to Hall probes just fractions of W away from the source and drain contacts.[19,20] This alone can lead to an underestimate of the Hall voltage by around 50%. The underestimate can be in excess of 80% when the invasiveness of the contacts is also taken into account. The contribution of (ii) only depends on the contact gap G_C compared to the sample width W and can be estimated using eqn (3). Estimating the contribution of (iii) is significantly more complicated because the current perturbation strongly depends not only on contact width and length but also on contact and sample resistance and even sample thickness. Here, eqn (3) can be used as a lower bound in estimating a correction factor because the reduction in measured Hall voltage will always be larger for invasive contacts. We provide a table of V_H^{sim}/V_H^{real} values for various sample geometries to help estimate the reduction in Hall voltage in the ESI.† Regardless, contact length and width should be decreased as much as possible to reduce the effect. Additionally, engineering probes to have higher contact resistance could reduce the current perturbation.

Overall, we find that Hall measurements even with invasive contacts, are a suitable way to characterize 2D nanostructures. However, care should be taken to minimize and correct for the associated reductions in measured Hall voltage. While the considerations in this paper focussed on III–V nanostructures, we expect them to be relevant for measurements on other 2D-nanostructures such as graphene[45] and transition metal dichalcogenides[10] with similar device geometries.

Conflicts of interest

There are no conflicts to declare.

Acknowledgements

This work was funded by the Australian Research Council (ARC) and the University of New South Wales. This work was performed in part using the NSW and ACT nodes of the Australian National Fabrication Facility (ANFF) and the Electron Microscope Unit (EMU) within the Mark Wainwright Analytical Centre (MWAC) at UNSW Sydney.

Notes and references

1 E. H. Hall, *Am. J. Math.*, 1879, **2**, 287–292.

2 K. v. Klitzing, G. Dorda and M. Pepper, *Phys. Rev. Lett.*, 1980, **45**, 494–497.
3 D. C. Tsui, H. L. Stormer and A. C. Gossard, *Phys. Rev. Lett.*, 1982, **48**, 1559–1562.
4 M. König, S. Wiedmann, C. Brüne, A. Roth, H. Buhmann, L. W. Molenkamp, X.-L. Qi and S.-C. Zhang, *Science*, 2007, **318**, 766–770.
5 T. Ihn, *Semiconductor Nanostructures: Quantum states and electronic transport*, Oxford University Press, 2009.
6 K. S. Novoselov, A. K. Geim, S. V. Morozov, D. Jiang, Y. Zhang, S. V. Dubonos, I. V. Grigorieva and A. A. Firsov, *Science*, 2004, **306**, 666–669.
7 K. S. Novoselov, A. K. Geim, S. V. Morozov, D. Jiang, M. I. Katsnelson, I. V. Grigorieva, S. V. Dubonos and A. A. Firsov, *Nature*, 2005, **438**, 197–200.
8 Q. H. Wang, K. Kalantar-Zadeh, A. Kis, J. N. Coleman and M. S. Strano, *Nat. Nanotechnol.*, 2012, **7**, 699–712.
9 S. Z. Butler, S. M. Hollen, L. Cao, J. A. Gupta, H. R. Gutiérrez, T. F. Heinz, S. S. Hong, J. Huang, A. F. Ismach, E. Johnston-Halperin, M. Kuno, V. V. Plashnitsa, R. D. Robinson, R. S. Ruoff, S. Salahuddin, J. Shan, L. Shi, M. G. Spencer, M. Terrones, W. Windl and J. E. Goldberger, *ACS Nano*, 2013, **7**, 2898–2926.
10 G. Nazir, M. F. Khan, V. M. Iermolenko and J. Eom, *RSC Adv.*, 2016, **6**, 60787–60793.
11 B. Radisavljevic and A. Kis, *Nat. Mater.*, 2013, **12**, 815–820.
12 B. Radisavljevic, A. Radenovic, J. Brivio, V. Giacometti and A. Kis, *Nat. Nanotechnol.*, 2011, **6**, 147–150.
13 A. Allain and A. Kis, *ACS Nano*, 2014, **8**, 7180–7185.
14 J. Seidl, J. G. Gluschke, X. Yuan, S. Naureen, N. Shahid, H. H. Tan, C. Jagadish, A. P. Micolich and P. Caroff, *Nano Lett.*, 2019, **19**, 4666–4677.
15 M. Borg, H. Schmid, J. Gooth, M. D. Rossell, D. Cutaia, M. Knoedler, N. Bologna, S. Wirths, K. E. Moselund and H. Riel, *ACS Nano*, 2017, **11**, 2554–2560.
16 C.-Y. Chi, C.-C. Chang, S. Hu, T.-W. Yeh, S. B. Cronin and P. D. Dapkus, *Nano Lett.*, 2013, **13**, 2506–2515.
17 D. Pan, J.-Y. Wang, W. Zhang, L. Zhu, X. Su, F. Fan, Y. Fu, S. Huang, D. Wei, L. Zhang, M. Sui, A. Yartsev, H. Xu and J. Zhao, *Nano Lett.*, 2019, **19**, 1632–1642.
18 D. Pan, D. X. Fan, N. Kang, J. H. Zhi, X. Z. Yu, H. Q. Xu and J. H. Zhao, *Nano Lett.*, 2016, **16**, 834–841.
19 N. Kang, D. Fan, J. Zhi, D. Pan, S. Li, C. Wang, J. Guo, J. Zhao and H. Xu, *Nano Lett.*, 2019, **19**, 561–569.
20 S. Gazibegovic, G. Badawy, T. L. J. Buckers, P. Leubner, J. Shen, F. K. de Vries, S. Koelling, L. P. Kouwenhoven, M. A. Verheijen and E. P. A. M. Bakkers, *Adv. Mater.*, 2019, **31**, 1808181.
21 Q. Sun, H. Gao, X. Zhang, X. Yao, S. Xu, K. Zheng, P. Chen, W. Lu and J. Zou, *Nanoscale*, 2020, **12**, 271–276.
22 A. Kelrich, O. Sorias, Y. Calahorra, Y. Kauffmann, R. Gladstone, S. Cohen, M. Orenstein and D. Ritter, *Nano Lett.*, 2016, **16**, 2837–2844.
23 M. de la Mata, R. Leturcq, S. R. Plissard, C. Rolland, C. Magén, J. Arbiol and P. Caroff, *Nano Lett.*, 2016, **16**, 825–833.
24 Z. Yang, A. Surrente, G. Tutuncuoglu, K. Galkowski, M. Cazaban-Carrazé, F. Amaduzzi, P. Leroux, D. K. Maude, A. Fontcuberta i Morral and P. Plochocka, *Nano Lett.*, 2017, **17**, 2979–2984.
25 S. Gazibegovic, D. Car, H. Zhang, S. C. Balk, J. A. Logan, M. W. A. de Moor, M. C. Cassidy, R. Schmits, D. Xu, G. Wang, P. Krogstrup, R. L. M. Op het Veld, K. Zuo, Y. Vos, J. Shen, D. Bouman, B. Shojaei, D. Pennachio, J. S. Lee, P. J. van Veldhoven, S. Koelling, M. A. Verheijen, L. P. Kouwenhoven, C. J. Palmstrøm and E. P. A. M. Bakkers, *Nature*, 2017, **548**, 434–438.
26 S. R. Plissard, I. van Weperen, D. Car, M. A. Verheijen, G. W. G. Immink, J. Kammhuber, L. J. Cornelissen, D. B. Szombati, A. Geresdi, S. M. Frolov, L. P. Kouwenhoven and E. P. A. M. Bakkers, *Nat. Nanotechnol.*, 2013, **8**, 859–864.
27 J. Gooth, M. Borg, H. Schmid, V. Schaller, S. Wirths, K. Moselund, M. Luisier, S. Karg and H. Riel, *Nano Lett.*, 2017, **17**, 2596–2602.
28 J. Gooth, M. Borg, H. Schmid, N. Bologna, M. D. Rossell, S. Wirths, K. Moselund, K. Nielsch and H. Riel, *Semicond. Sci. Technol.*, 2019, **34**, 035028.
29 M. Friedl, K. Cerveny, C. Huang, D. Dede, M. Samani, M. O. Hill, N. Morgan, W. Kim, L. Güniat, J. Segura-Ruiz, L. J. Lauhon, D. M. Zumbühl and A. Fontcuberta i Morral, *Nano Lett.*, 2020, **20**, 3577–3584.
30 D. B. Suyatin, C. Thelander, M. T. Björk, I. Maximov and L. Samuelson, *Nanotechnology*, 2007, **18**, 105307.
31 C. Blömers, T. Grap, M. I. Lepsa, J. Moers, S. Trellenkamp, D. Grützmacher, H. Lüth and T. Schäpers, *Appl. Phys. Lett.*, 2012, **101**, 152106.
32 C. Durand, M. Berthe, Y. Makoudi, J.-P. Nys, R. Leturcq, P. Caroff and B. Grandidier, *Nanotechnology*, 2013, **24**, 275706.
33 K. Storm, F. Halvardsson, M. Heurlin, D. Lindgren, A. Gustafsson, P. M. Wu, B. Monemar and L. Samuelson, *Nat. Nano*, 2012, **7**, 718–722.
34 J. R. Sambles and K. C. Elsom, *Solid State Commun.*, 1984, **52**, 367–370.
35 H. Schmid, M. Borg, K. Moselund, L. Cignac, C. M. Breslin, J. Bruley, D. Cutaia and H. Riel, *Appl. Phys. Lett.*, 2015, **106**, 233101.
36 K. Seeger, *Semiconductor Physics: An Introduction*, Springer, Berlin, 8th edn, 2010.
37 M. J. L. Sourribes, I. Isakov, M. Panfilova and P. A. Warburton, *Nanotechnology*, 2013, **24**, 045703.
38 J. P. DeGrave, D. Liang and S. Jin, *Nano Lett.*, 2013, **13**, 2704–2709.
39 F. Haas, P. Zellekens, M. Lepsa, T. Rieger, D. Grützmacher, H. Lüth and T. Schäpers, *Nano Lett.*, 2017, **17**, 128–135.
40 V. E. Degtyarev, S. V. Khazanova and N. V. Demarina, *Sci. Rep.*, 2017, **7**, 3411.
41 J. Salfi, N. Paradiso, S. Roddaro, S. Heun, S. V. Nair, I. G. Savelyev, M. Blumin, F. Beltram and H. E. Ruda, *ACS Nano*, 2011, **5**, 2191–2199.

42 G. W. Holloway, Y. Song, C. M. Haapamaki, R. R. LaPierre and J. Baugh, *J. Appl. Phys.*, 2013, **113**, 024511.
43 I.-J. Chen, S. Lehmann, M. Nilsson, P. Kivisaari, H. Linke, K. A. Dick and C. Thelander, *Nano Lett.*, 2017, **17**, 902–908.
44 M. Nilsson, L. Namazi, S. Lehmann, M. Leijnse, K. A. Dick and C. Thelander, *Phys. Rev. B*, 2016, **93**, 195422.
45 X. Du, I. Skachko, F. Duerr, A. Luican and E. Y. Andrei, *Nature*, 2009, **462**, 192–195.